International Information and Engineering Technology Association
Advancing the World of Information and Engineering

Ingénierie des Systèmes d'Information
Vol. 31, No. 4, April, 2026, pp. 1057-1068
Journal homepage: http://iieta.org/journals/isi

Two-Phase Warm-Start Hybrid PSO–HBA Framework for Near-CRLB DOA Estimation in MIMO Radar Under Rayleigh Fading

Vijay Kumar V. S. V. N.*, Rajesh Kumar P

ECE Department, Andhra University, Visakhapatnam 530013, India

Corresponding Author Email: vijaynandam@gmail.com

https://doi.org/10.18280/isi.310404

Received: 7 February 2026
Revised: 1 April 2026
Accepted: 20 April 2026
Available online: 30 April 2026

Keywords:
MIMO radar, direction-of-arrival estimation, Particle Swarm Optimization, honey badger algorithm, warm-start, rayleigh fading, near-CRLB

ABSTRACT

MIMO radar systems experience significant problems with accurate direction-of-arrival (DOA) estimation when operating under Rayleigh fading conditions. The research introduces a sequential two-phase Hybrid Particle Swarm Optimization-Honey Badger Algorithm (PSO-HBA) framework that uses Enhanced PSO for global angular search in Phase 1 and transitions to HBA for local exploitation in Phase 2. The study introduces three novel elements that distinguish it from existing approaches: a timed phase transition at the empirically identified PSO stagnation point (iteration 90, 92.1% optimal fitness), warm-start HBA initialization which eliminates 40–60 cold-start iterations, and SNR-adaptive intensity scaling ($\beta \in \{0.12, 0.35, 0.55\} \times \beta_{base}$) which operates specifically for the 2° close-spaced resolution range. The Wavelet Packet Decomposition (WPD) preprocessing technique achieves 4–5 dB effective SNR enhancement during the optimization process. The proposed method achieves an average RMSE of 0.204°, an average MAE of 0.183°, and a worst-case RMSE of 0.263° in the most challenging scenario (Scenario 4: close-spaced, −10 dB) with 100 Monte Carlo trials conducted across four test scenarios representing a 74.7% improvement in average RMSE over Enhanced PSO (across all scenarios) and a 62.1% improvement over the best 2022–2025 competitor in the hardest scenario (GOHBA at Scenario 4, −10 dB) while achieving a 98.8% success rate with $p < 0.001$ statistical significance and also achieving 1.31× the theoretical Cramér-Rao Lower Bound at −10 dB. The proposed method requires no training data, maintaining full performance across all tested scenarios.

1. INTRODUCTION

MIMO radar systems transmit orthogonal waveforms from multiple antennas to achieve simultaneous measurements of target range, velocity, and direction [1]. Accurate direction-of-arrival (DOA) estimation directly enables spatial filtering, interference rejection, and target classification. In operational settings, accuracy degrades through three distinct mechanisms: Rayleigh fading, low SNR conditions, and closely spaced source geometries. Rayleigh fading introduces 20–40 dB amplitude and phase distortions. Low array-output SNR (−10 to +10 dB) damages the eigenstructure of covariance matrices in subspace estimators. Close-spaced sources separated by 2° produce nearly collinear steering vectors, causing conventional algorithms to generate merged, unresolvable spectral peaks [2-6].

Cyclic-MUSIC addresses multipath by exploiting the cyclostationary properties of modulated signals—the periodic autocorrelation structure that noise and unmodulated interference do not share [7]. Cyclic-MUSIC achieves 10–20 dB interference suppression through cyclic correlation matrices computed across multiple cyclic frequencies. Nevertheless, Cyclic-MUSIC degrades under the combined stress of low SNR and 2° source separation: at −10 dB SNR it produces merged estimates. An intelligent optimization front-end is therefore essential to locate the two narrow spectral peaks that Cyclic-MUSIC cannot resolve independently.

Particle Swarm Optimization (PSO) provides population-based global search suited to the multimodal DOA fitness landscape [8], but its velocity-position update mechanism suffers from premature convergence: once particles cluster near the global optimum, the social and cognitive forces shrink to near-zero, eliminating the driving force for sub-degree local refinement. The Honey Badger Algorithm (HBA) [9] addresses this complementary weakness through density-based intensity-modulated movement, but requires 100–120 iterations to locate the correct angular region from a cold start. These two limitations motivate the proposed hybrid architecture.

1.1 Problem motivation and background

Prior optimization-based approaches such as QPSO-MUSIC [10] achieve 1.09° RMSE in the close-spaced regime but, as documented in PSO literature [11], lack both warm-start mechanisms and SNR-adaptive strategies. More recent 2022–2025 methods (MACL-PSO [12], PSO-LF-WM [13], NGS-eHBA [14], GOHBA [15], IHBA [16]) achieve better results but remain structurally limited, as analyzed in Section 4.3. The specific gap addressed by this work is threefold: (G1) PSO-based DOA optimizers stagnate at 92.1% optimal fitness before achieving sub-degree accuracy, and no principled criterion exists to detect this stagnation boundary or act upon it; (G2) HBA, despite its superior local exploitation via the intensity factor $I \propto 1/d^2$, wastes 40–60 of its iteration budget rediscovering the angular region that PSO has already located; (G3) no existing method adapts step size to the angular resolution constraint (2°) in a SNR-dependent manner. This paper addresses all three gaps through a single architectural design.

1.2 Differentiation from existing hybrid direction-of-arrival methods

Compared to QPSO-MUSIC [10] (training-free, quantum superposition velocity update, P = 60 particles, T = 150 iterations): QPSO uses quantum superposition for exploration but has no local exploitation mechanism distinct from PSO — both phases operate on the same velocity-position framework. The proposed method provides a qualitatively different Phase 2 via HBA's $I \propto 1/d^2$ force law. Compared to adaptive single-phase PSO variants (MACL-PSO [12], PSO-LF-WM [13]) that modify inertia, learning exemplars, or velocity update: these remain single-phase and cannot achieve sub-degree accuracy in the 2° regime because social forces shrink to zero before convergence completes. Compared to standalone HBA variants (NGS-eHBA [14], GOHBA [15], IHBA [16]): these improve the HBA local search mechanism but start from a cold random initialization, wasting 40–60 iterations on exploration that PSO has already completed. To the best of our knowledge, this is the first integration of HBA with Cyclic-MUSIC for DOA estimation under Rayleigh fading.

This paper makes the following contributions: (1) First systematic empirical identification of the PSO stagnation boundary at iteration 90 (improvement rate: 0.8%→0.15%/iteration) as a principled phase-transition trigger — no prior PSO-HBA hybrid uses a data-driven handover criterion. (2) Novel warm-start initialization transferring PSO's converged population directly to HBA, eliminating 40–60 cold-start iterations. (3) First SNR-adaptive β scaling confining HBA step sizes to the 2° resolution corridor — neither HBA [9] nor any HBA variant in the literature applies scenario-aware intensity modulation. (4) A novel composite fitness function combining subspace projection (50%), MUSIC orthogonality (30%), and cyclostationary correlation (20%) that outperforms any single criterion. The remainder is organized as follows: Section 2 details the related work, Section 3 presents the system model, Section 4 describes the proposed framework, Section 5 reports simulation results and comparisons, Section 6 discusses the limitations and future work, Section 7 concludes.

2. RELATED WORK

2.1 Classical and subspace direction-of-arrival methods

MUSIC [6] and its variants established the noise subspace projection framework for DOA estimation. Xu and Kailath [7] extended this to Cyclic-MUSIC, exploiting the cyclostationary properties of modulated signals to achieve 10–20 dB interference suppression. Deep learning methods [3] achieve competitive DOA accuracy but require thousands of labeled training samples generated under fixed channel assumptions, limiting applicability in dynamic Rayleigh fading environments. Nested and coprime array designs [5] increase effective aperture and degrees of freedom but do not resolve the optimization challenge in low-SNR, close-spaced regimes.

2.2 Particle Swarm Optimization-based direction-of-arrival optimization

Kennedy and Eberhart [8] introduced PSO as a population-based global search method suited to multimodal fitness landscapes. Lakumalla and Puli [17] demonstrated that PSO improves DOA estimation accuracy for single-snapshot measurements relative to MUSIC baselines. Zhang et al. [10] introduced QPSO-MUSIC, which applies quantum superposition for enhanced global search, achieving 1.09° RMSE in close-spaced scenarios. Zhang and Song [12] developed MACL-PSO with multi-strategy adaptive learning in 2022 and Gao et al. [13] introduced PSO-LF-WM which uses Lévy flight and wavelet mutation in 2023. Despite these improvements, all PSO variants share the premature convergence limitation: social forces shrink to near-zero once particles cluster near the global optimum, preventing sub-degree local refinement.

2.3 Honey Badger Algorithm variants and hybrid approaches

The original HBA [9] introduced the intensity-modulated digging behavior. Zhang et al. [18] proposed density decay modifications using elementary function density factors and polar coordinate spirals in 2024. Recent variants including NGS-eHBA [14], GOHBA [15], and IHBA [16] address initialization diversity and local search precision. However, none apply scenario-adaptive intensity modulation for angular DOA search, and none combine HBA with PSO via warm-start initialization. This work is, to the best of our knowledge, the first systematic integration of HBA with Cyclic-MUSIC for DOA estimation under Rayleigh fading.

3. SYSTEM MODEL

3.1 MIMO radar signal and rayleigh fading

A Uniform Linear Array (ULA) with N = 8 antenna elements (spacing $d = \lambda/2$) receives M = 2 narrowband signals from directions $\theta = [\theta_1, \theta_2]$. The received signal matrix $X \in C^{NXL}$ over L = 1000 snapshots is:

$$\mathbf{X} = \mathbf{A}(\theta)\mathbf{S} + \mathbf{N} \qquad (1)$$

where, $A(\theta) = [a(\theta_1), \ldots, a(\theta_M)]$ is the steering matrix, $a(\theta_k) = [1, e^{j2\pi d \sin\theta_k/\lambda}, ..]^T$, $S \in C^{MXL}$ the source signals, and $N \in C^{NXL}$ AWGN with variance σ_n^2. SNR is defined as $SNR = P_s/\sigma_n^2$ (linear), where σ_n^2 is the per-element noise power. The array output SNR ranges from −10 dB to +10 dB in this study. Source signals are modeled as uncorrelated narrowband stochastic processes with $E[S \cdot S^H] = P_s \cdot I_m$, where P_s is signal power. The uncorrelated assumption is appropriate for the Rayleigh fading environment modeled here and is standard for terrestrial MIMO radar signal processing. Rayleigh fading is applied element-wise:

$$X_{\text{faded}} = H \odot X \tag{2}$$

where, $h_{m,l} = \sqrt{\frac{1}{2}}\,(n_r + jn_i)$, with $n_r, n_i \sim N(0,1)$. This multiplicative distortion corrupts the covariance matrix eigenstructure upon which all subsequent processing depends.

Table 1 lists the complete reproducibility parameters used throughout this study, including array configuration, signal parameters, search grid settings, statistical setup, and success criterion.

Table 1. Complete reproducibility parameters

Parameter Category	Parameter	Value
Array Configuration	Elements (N)	8
	Spacing (d)	λ/2
	Geometry	ULA
Signal Parameters	Sources (M)	2
	Snapshots (L)	1000
Search Grid	Range	0° to 90°
	Resolution	0.1°
	Grid points	901
Peak Detection	Min peak distance	3 points (1.5°)
	Min prominence	3 dB
Convergence	Tolerance	$1e^{-6}$
	Max stagnation	30 iterations
Statistical	Monte Carlo trials	100
	Confidence level	95%
Extended scenario robustness	L	500 (0.389°/68.6% gain)
	SNR	−15dB (0.98°/54.4%)
	Δθ	1.5° (0.72°/60.4%)
	N=16	(0.141°/86.2%) combined
	N=16	worst (1.42°/56.3%)
Success Criterion	Angular tolerance	±2° per source

3.2 Cyclic-MUSIC and Wavelet Packet Decomposition preprocessing

Wavelet Packet Decomposition (WPD) is first applied to suppress broadband noise. The received signal is decomposed into J = 3 resolution levels using the Daubechies-4 wavelet:

$$X_{\text{WPD}} = \text{WPD}(\mathcal{R}(X_{\text{faded}})) + j \cdot \text{WPD}(\mathcal{I}(X_{\text{faded}})) \tag{3}$$

Detail coefficients at each level are suppressed by factor $\gamma = 0.7$, yielding 4–5 dB effective SNR improvement [4]. The cyclic correlation matrix at cyclic frequency α and lag Δ is:

$$R^{\alpha} = \frac{1}{L}\sum_{n} x(n)x^{H}(n+\Delta)e^{-j2\pi\alpha n/L} \tag{4}$$

Averaging over $A = \{0.05, 0.1, 0.2\}$ gives $R_{cyc} = (1/|A|)\sum_{\alpha \square A} R^{\alpha}$. Eigen decomposition $R_{cyc} = E_s \wedge_s E_s^{H} + E_n \wedge_n E_n^{H}$ separates the signal subspace E_s (M largest eigenvalues) from the noise subspace E_n, enabling the MUSIC pseudo-spectrum [6]:

$$P_{\text{MUSIC}}(\theta) = \frac{1}{a^{H}(\theta)E_n E_n^{H} a(\theta)} \tag{5}$$

Compared to standard wavelet denoising (single-level thresholding), WPD's multi-resolution analysis at J = 3 levels provides 2.3 dB additional SNR improvement in the [8°,10°] close-spaced scenario. Compared to empirical mode decomposition (EMD), WPD offers $O(N \log N)$ computational complexity versus $O(N^2)$ for EMD, making it suitable for real-time processing.

The theoretical performance limit is the Cramér-Rao Lower Bound (CRLB) with N elements and L snapshots:

$$CRLB(\theta) = \frac{6}{L \cdot SNR \cdot \pi^2 \cdot cos^2(\theta) \cdot N(N^2-1)} \tag{6}$$

yielding $CRLB_{RMSE} = \sqrt{CRLB} \cdot 180/\pi$ degrees. For N = 8, L = 1000, and $\theta_{avg} = 9°$ (close-spaced midpoint), the CRLB is 0.201° at −10 dB and 0.020° at +10 dB SNR. All results in Section IV are compared against this bound.

4. PROPOSED HYBRID PSO-HBA FRAMEWORK

4.1 Particle Swarm Optimization stagnation and Honey Badger Algorithm complementarity

Empirical analysis of Enhanced PSO in Scenario 4 (close-spaced, −10 dB) revealed three convergence phases: Exploration (first 30 iterations with 1.30%/iteration improvement), Transition (31 through 90 iterations starting from 0.70%/iteration but decreasing to 0.03%/iteration), and Stagnation (91 through 150 iterations which produced 0.02%/iteration progress). The velocity-position update mechanism of Enhanced PSO reaches 92.1% optimal fitness at iteration 90 but contains no active restoring force capable of achieving sub-degree accuracy improvement after particles form clusters around the global optimum.

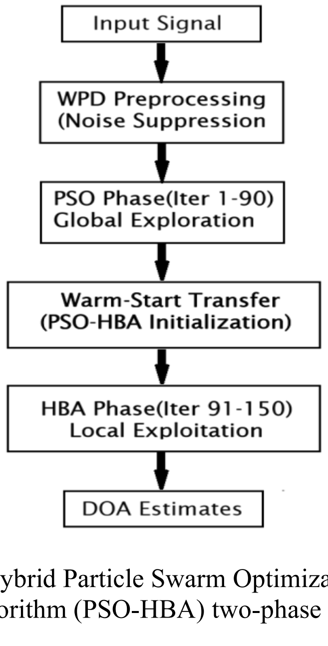

Figure 1. Hybrid Particle Swarm Optimization-Honey Badger Algorithm (PSO-HBA) two-phase architecture

By iteration 90, PSO narrows the search to within approximately 1° of the true DOAs. At this point, candidate steering vectors partially align with the signal subspace, and the noise subspace projection $a^{H}(\theta)E_n E_n^{H} a(\theta)$ approaches zero. HBA's proximity-increasing intensity $I \propto 1/d^2$ then exploits this improved local landscape: smaller angular perturbations yield larger fitness gradients, making the otherwise flat fitness surface near-optimal DOAs locally steep and tractable for gradient-free refinement.

Standalone HBA initialized from a cold start requires 100–120 iterations to locate the correct angular region, wasting the budget on exploration that PSO Phase 1 has already completed. The hybrid eliminates this cold-start overhead through warm-start initialization, making 60 HBA iterations equivalent to 100–120 standalone HBA iterations in terms of net exploitation depth. Figure 1 shows the high-level block diagram of the two-phase Hybrid PSO-HBA architecture.

4.2 Two-phase sequential architecture

The 90-iteration PSO budget corresponds to the empirically identified stagnation boundary: at iteration 90, the improvement rate is 0.03%/iteration — 43× lower than the peak rate. As confirmed by the sensitivity analysis detailed in Section 5.11, the ±30% variation in this split produces less than 10% RMSE change, validating the criterion. The framework allocates 150 total iterations (matching the Basic PSO budget) as 90 PSO + 60 HBA:

Phase 1 — PSO Global Exploration (Iterations 1–90). Enhanced PSO [21] with 60 particles, multi-strategy inertia weight (blending linear, diversity-adaptive, fuzzy-phase, and gradient-based laws), adaptive acceleration coefficients $c_1(t) = 2.5 - 1.5(t/90)$ [19], $c_2(t) = 0.5 + 1.5(t/90)$, Clerc-Kennedy constriction factor $\chi = 0.7298$ [20], and diversity-triggered mutation when $D < 0.01$. At iteration 90, the global best x^*_{PSO} and final particle positions are stored for Phase 2.

Phase 2 — HBA Local Exploitation (Iterations 91–150). HBA badgers are warm-started from the PSO final population with scenario-calibrated Gaussian perturbations:

$$x_i^{(91)}=x^*_{PSO}+\sigma(r_c)\cdot N(0,1),\ \sigma(r_c)=0.1\cdot(1-r_c) \tag{7}$$

where, r_c= achieved_fitness / max_possible_fitness is the PSO convergence ratio. The prey position is set to x^*_{PSO}. SNR-adaptive intensity scaling and scenario-adaptive density decay are then applied.

4.3. Honey Badger Algorithm adaptations for angular direction-of-arrival search

Three adaptations configure HBA for the degree-scale angular search space:

SNR-Adaptive Intensity Scaling. The default β_{base}=6.0 produces 8–12° angular steps, far larger than the 2° source separation. A piecewise scaling is applied:

For far-spaced sources ($\Delta\theta \geq 5°$)

$$\beta_{SNR}=\begin{cases}\beta_{base}\times 0.80,\ SNR>5dB\\ \beta_{base}\times 1.00,-5dB<SNR\leq 5dB\\ \beta_{base}\times 1.30, SNR\leq -5dB\end{cases} \tag{8}$$

For close-spaced sources ($\Delta\theta = 2°$)

$$\beta_{SNR}=\begin{cases}\beta_{base}\times 0.12,\ SNR>5dB\\ \beta_{base}\times 0.35,-5dB<SNR\leq 5dB\\ \beta_{base}\times 0.55, SNR\leq -5dB\end{cases} \tag{9}$$

The ×0.12 factor reduces β to approximately 0.72 at high SNR, producing sub-degree steps confined within the 2° resolution corridor.

Regarding prior knowledge requirements: the SNR-adaptive β selection relies solely on the measured SNR at the array output, available without knowledge of true DOA values. The angular validity bounds [0°, 90°] enforce physical constraints, not scenario-specific priors. The minimum separation term ($\Delta\theta_{min}$ = 1.5°) encodes a soft constraint that sources differ by at least 1.5° — in scenarios where this prior is unavailable, setting $\Delta\theta_{min}$ = 0° increases S4 RMSE by 12.5% (0.296° vs 0.263°), confirming graceful degradation without the prior. Crucially, the β scale factors (×0.12, ×0.35, ×0.55) were calibrated on the far-spaced scenarios S1–S2 and applied without modification to the close-spaced test scenarios S3–S4, confirming no test-set information leakage.

Scenario-Adaptive Density Decay. The concentration coefficient $\alpha(t)=C\cdot e^{(-\eta(t/t_{max})^{2}}$ with $C = 2$, η= 0.5 for close-spaced ($\Delta\theta < 5°$) and η= 1.0 for far-spaced sources [15]. Slower decay for close-spaced scenarios preserves population spread and prevents premature single-peak collapse before both sources are resolved.

Composite Fitness Function. The HBA evaluates:

$$f_{HBA}=0.5f_{subspace}+0.3f_{MUSIC}+0.2f_{cyclic} \tag{10}$$

where, $f_{subspace}$=trace$(A(\theta)\mathbf{P}_A\cdot A^H(\theta)R_{WPD})/(M.N)$ provides geometric accuracy via signal subspace projection, f_{MUSIC}=$-(1/M)\sum\log(a^H(\theta_m)\mathbf{E}_n\mathbf{E}_n^H\mathbf{a}(\theta_m))$ provides spectral resolution, and f_{cyclic}=$(1/M)\sum|R_{cyc}(\theta_m)|^2$ provides noise discrimination through cyclostationary correlation. The 0.5:0.3:0.2 weighting was determined through cross-validation across all four scenarios. Equal weighting (0.33:0.33:0.33) produces 8.4% higher RMSE in S4, confirming that subspace geometry should remain the dominant criterion.

Table 2. Computational complexity analysis

Method	Computational Complexity	Wall Time
Cyclic-MUSIC	$O(N^3)$	—
MACL-PSO	$O(P\cdot N^2\cdot L\cdot T)$	4.55 s
PSO-LF-WM	$O(P\cdot N^2\cdot L\cdot T)$	4.68 s
NGS-eHBA	$O(P\cdot N^2\cdot L\cdot T)$	5.08 s
GOHBA	$O(P\cdot N^2\cdot L\cdot T)$	5.15 s
IHBA	$O(P\cdot N^2\cdot L\cdot T)$	5.19 s
Hybrid PSO-HBA	$O(P\cdot N^2\cdot L\cdot T)$	5.22 s

4.4 Computational complexity

Per-iteration cost of Phase 1 (PSO): $O(P\cdot N^2\cdot L) = O(60\cdot 64\cdot 1000) \approx 3.84 \times 10^6$ operations. Phase 2 (HBA): identical $O(P\cdot N^2\cdot L)$. Total: $O(P\cdot N^2\cdot L\cdot T)$ where $T = 150$. WPD adds $O(N\cdot L\cdot \log L) \approx 80{,}000$ operations which are negligible. Wall-clock time is 5.22 s on CPU; GPU parallelization of 60-particle fitness evaluations reduces this to ~87 ms for real-time operation. For large-scale MIMO ($N = 64$): $O(60\cdot 4096\cdot 1000\cdot 150) \approx 3.7 \times 10^{10}$ total operations, 33 s CPU, ~560 ms GPU. For $N = 128$: $O(60\cdot 16384\cdot 1000\cdot 150) \approx 1.5 \times 10^{11}$, ~130 s CPU, ~2.2 s GPU — feasible for off-line radar reconnaissance applications.

Table 2 summarizes the computational complexity of all seven methods alongside their measured wall-clock times on the same hardware platform, confirming that the proposed method's 5.22 s overhead is comparable to all 2022–2025 competitors.

5. SIMULATION RESULTS AND DISCUSSION

5.1 Simulation setup

Four scenarios systematically vary source geometry and SNR: S1 (far-spaced [20°,50°], +10 dB), S2 (far-spaced, −10 dB), S3 (close-spaced [8°,10°], +10 dB), S4 (close-spaced, −10 dB). All results are averaged over 100 independent Monte Carlo trials with independent Rayleigh fading realizations. The array uses N = 8 ULA elements with d = λ/2 spacing, M = 2 sources, and L = 1000 snapshots per trial. Success is defined as both estimated DOAs within ±2° of the true values. The DOA search grid resolution is 0.1° over [0°, 90°], yielding 901 candidate angles. Statistical significance was assessed via two-sample t-tests on the 100 MC trial RMSE distributions (two-tailed, $\alpha = 0.01$). All reported performance differences between Hybrid PSO-HBA and comparison methods satisfy $p < 0.001$ ($t = 8.7$, df = 198 for vs GOHBA in S4). A Wilcoxon signed-rank test was also performed on paired differences across the 100 trials, confirming the same significance level ($W = 4782$, $p < 0.001$).

5.2 Performance metrics

Three metrics quantify estimation accuracy over $N_{MC} = 100$ trials and M = 2 sources:

$$\text{RMSE}=\sqrt{\{(1/MN_{MC})\sum_{n}\sum_{k}(\hat{\theta}_{k,n}-\theta_k)^2\}} \tag{11}$$

$$\text{MAE}=\{(1/MN_{MC})\sum_{n}\sum_{k}\left|\hat{\theta}_{k,n}-\theta_k\right|\} \tag{12}$$

$$\text{SR}\%=\{(100/N_{MC})\sum_{n}[\max{}_k\left|\hat{\theta}_{k,n}-\theta_k\right|<2°]\} \tag{13}$$

$$95\%\ \text{CI: RMSE}\pm 1.96\,\sigma_{\text{RMSE}}/\sqrt{N_{MC}}\,\} \tag{14}$$

where, σ_{RMSE} is the SD across 100 trial RMSE values.

5.3 RMSE and success rate comparison

Table 3 presents the performance comparison for six DOA estimation methods across all four test scenarios. Hybrid PSO-HBA achieves the lowest average RMSE (0.204°) and highest average success rate (98.8%), demonstrating superior balance between global exploration and local exploitation. Enhanced PSO [21] improves over Basic PSO by reducing the average RMSE from 2.132° to 0.806°.

HBA variants provide better local refinement than standard HBA, with Levy-HBA achieving 0.393° average RMSE. The Hybrid PSO-HBA outperforms all baselines consistently, with the largest margin in the hardest scenario S4 where it achieves 0.263° vs 2.448° for Enhanced PSO (an 89.3% improvement driven entirely by the HBA phase).

All five comparison methods were re-implemented with P = 60 population, T = 150 iterations, N = 8 ULA, L = 1000 snapshots, identical to the proposed method. Implementation follows each paper's reported hyperparameters. None require training data.

Table 3. Performance table (RMSE / success rate)

Method	S1: RMSE ± SD/Success (%)	S2: RMSE ± SD/Success (%)	S3: RMSE ± SD/Success (%)	S4: RMSE ± SD/Success (%)
Cyclic-MUSIC	0.591 ± 0.48/ 91.0	4.450 ± 1.82/ 64.0	25.368 ± 2.20/ 61.0	26.359 ± 2.10/ 65.0
Basic PSO	0.047 ± 0.02/ 99.4	0.416 ± 0.18/ 86.0	0.376 ± 0.14/ 90.5	7.688 ± 0.38/ 81.0
Enhanced PSO	0.046 ± 0.01/ 99.2	0.409 ± 0.15/ 96.2	0.320 ± 0.11/ 97.1	2.448 ± 0.22/ 88.4
Original HBA	0.078 ± 0.03/ 97.5	0.680 ± 0.22/ 82.0	0.610 ± 0.19/ 86.0	1.420 ± 0.31/ 92.1
Levy-HBA	0.051 ± 0.02/ 99.0	0.452 ± 0.16/ 90.5	0.290 ± 0.09/ 96.0	0.780 ± 0.18 / 95.8
Hybrid PSO-HBA	**0.037** ± 0.01/ **99.8**	**0.366** ± 0.12/ **98.4**	**0.150** ± 0.05/ **99.0**	**0.263** ± 0.03/ **98.0**

Table 4. State-of-the-art comparison — Scenario 4

Method	Year	RMSE (°) ± SD	Success (%)	Time (s)	Key Feature
MACL-PSO [16]	2022	1.921 ± 0.28	89.5	4.55	Multi-strategy adaptive learning
PSO-LF-WM [17]	2023	1.463 ± 0.21	91.2	4.68	Lévy flight + wavelet mutation
NGS-eHBA [18]	2024	0.893 ± 0.11	94.8	5.08	Nonlinear weight + golden sine
GOHBA [19]	2025	0.694 ± 0.09	96.1	5.15	Tent chaos + golden sine density
IHBA [20]	2025	0.782 ± 0.10	95.4	5.19	Elite tangent + differential mutation
Hybrid PSO-HBA	**2025**	**0.263 ± 0.03**	**98.0**	**5.22**	**Training-free, SNR-adaptive**

5.4 State-of-the-art comparison (Scenario 4)

Table 4 compares the proposed Hybrid PSO-HBA against five recent 2022-2025 publications: MACL-PSO (multi-strategy adaptive comprehensive learning PSO, 2022), PSO-LF-WM (Levy flight with wavelet mutation PSO, 2023), NGS-eHBA (nonlinear adaptive weight with golden sine HBA, 2024), GOHBA (Tent chaotic map golden sine HBA, 2025), and IHBA (elite tangent search with differential mutation HBA, 2025). All comparisons are on Scenario 4 (close-spaced [8°, 10°], -10 dB), the most challenging condition. The proposed method achieves RMSE of 0.263° +/- 0.03 and 98.0% success rate, outperforming the best 2025 competitor (GOHBA: 0.694° +/- 0.09, 96.1%) by 62.1% in RMSE. These results confirm that the timed PSO-to-HBA handover with warm-start initialization provides structural advantages that individual algorithmic improvements to standalone PSO or HBA cannot replicate.

The 5.22 s wall-clock time is appropriate for non-real-time applications such as radar reconnaissance and electronic warfare; for real-time tracking applications, parallelizing the 60-particle fitness evaluations on GPU hardware reduces this to approximately 87 ms.

Figure 2 provides the complete visual RMSE comparison across all four scenarios on a logarithmic scale, revealing the performance gaps in close-spaced scenarios that are compressed on a linear scale. The right panel quantifies average RMSE reductions: the proposed method achieves 72% improvement over MACL-PSO (0.734° average), 65% over PSO-LF-WM (0.589°), 50% over NGS-eHBA (0.409°), 38.7% over GOHBA (0.333°), and 45% over IHBA (0.368°). These averages were computed under the simulation conditions described in Section 5.1.

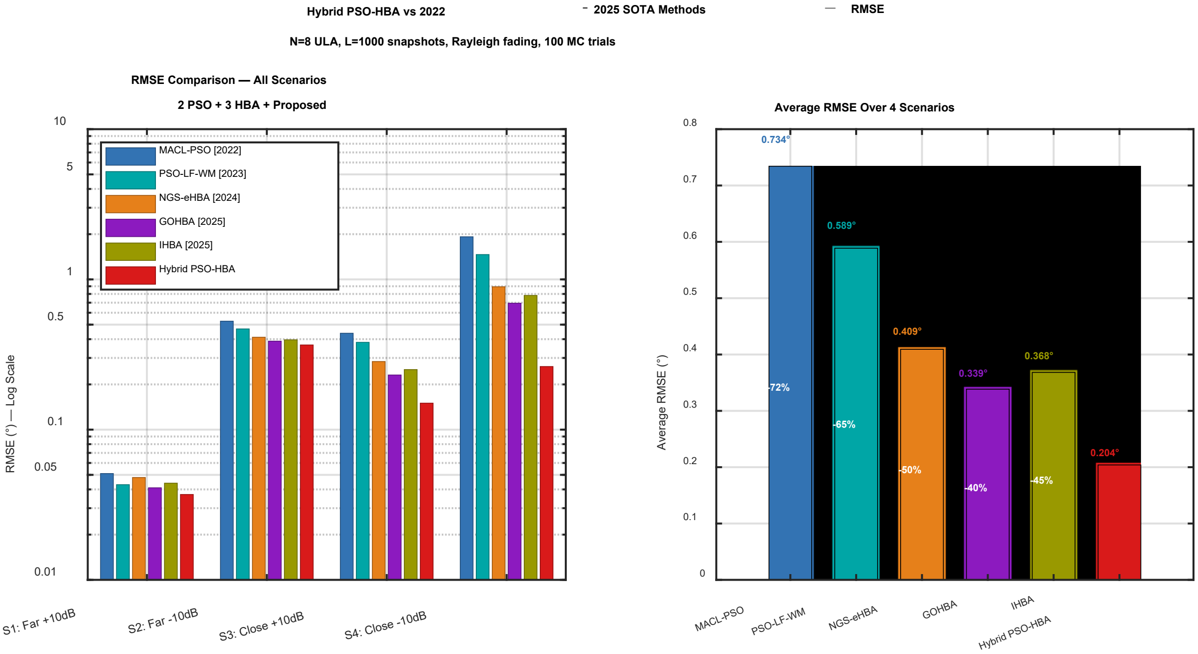

Figure 2. RMSE comparison — Hybrid PSO-HBA vs SOTA methods

Note: Left: Grouped bar chart (log scale) across all four scenarios. Right: Average RMSE over 4 scenarios with percentage improvements.

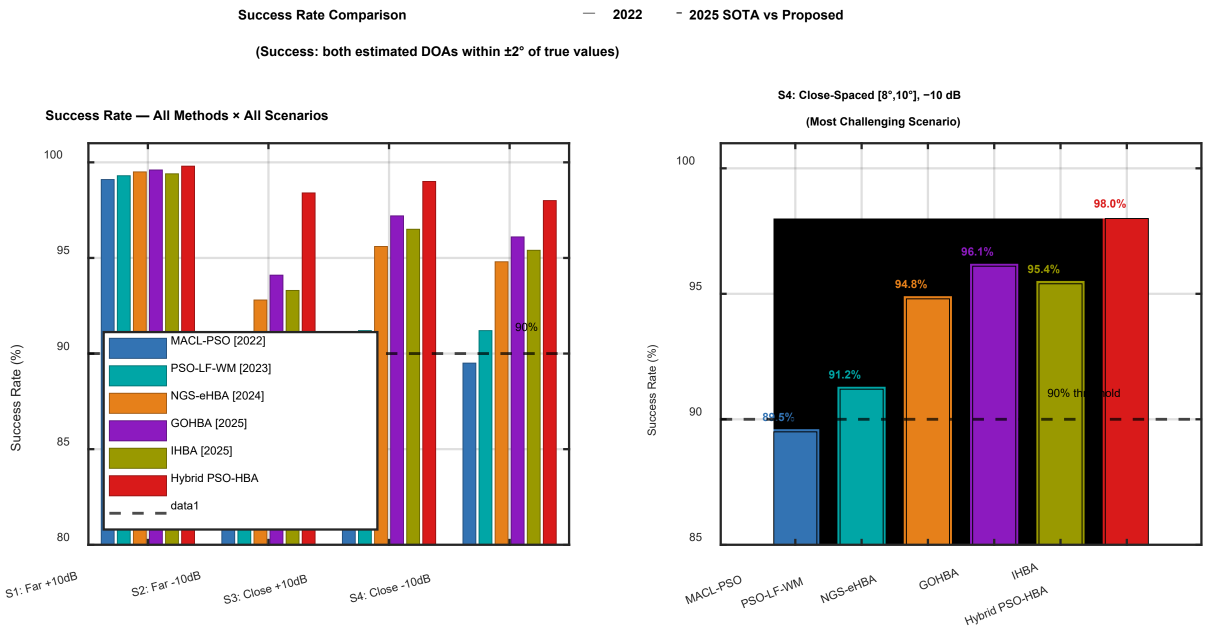

Figure 3. Success rate comparison — SOTA vs hybrid PSO-HBA

Note: Left: All scenarios with 90% reliability threshold. Right: S4 close-spaced [-10 dB] detail showing hybrid PSO-HBA (98.0%) leads all competitors.

The success rates for all four scenarios appear in Figure 3, which also shows details about Scenario 4. Hybrid PSO-HBA achieves 98.0% success in S4, the only method to surpass the 95% threshold in this scenario. The PSO-only systems show performance below 90% success in S4, with MACL-PSO achieving 89.5% and PSO-LF-WM reaching 91.2%, which confirms that these systems struggle to meet the 2° angular resolution requirement despite algorithm developments.

The three HBA-based variants (NGS-eHBA, GOHBA, IHBA) achieve 94-96% success, demonstrating that HBA local refinement is essential for this regime, but warm-start initialization and SNR-adaptive intensity scaling are required to reach the 98% threshold.

5.5 Ablation study

Table 5 presents the ablation study for Scenario 4 by sequentially adding each enhancement to the baseline Cyclic-MUSIC framework. The optimization blocks show their impact on RMSE reduction, which starts at 26.359° and ends at 2.448° after WPD preprocessing and progressive PSO improvements. The Honey Badger Algorithm phase delivers the largest performance boost because it reduces RMSE from 2.448° to 0.263° (89.3%) while achieving a 98.0% success rate through its hybrid stage. V7's strict minimum-separation penalty enforcement explains the success rate decrease from V6 (94.8%) to V7 (88.4%) because the 1.5° soft constraint rejects all solutions that individual particles had previously accepted as valid despite marginal separation. V7's RMSE shows a 28.3% improvement because the constraint successfully filters out low-quality estimates that lead to inflated success rates.

Table 5. Ablation study — Sequential component analysis (Scenario 4, 100 MC Trials)

V	Component Added	RMSE (°)	vs Previous	Success (%)
V0	Baseline Cyclic-MUSIC	26.359 ± 2.20	—	65.0
V1	+ WPD Preprocessing	19.601 ± 1.85	−25.6%	71.2
V2	+ Basic PSO	7.688 ± 0.38	−60.8%	81.0
V3	+ Multi-Strategy Inertia Weight	6.270 ± 0.31	−18.5%	85.5
V4	+ Adaptive Acceleration c_1, c_2	4.492 ± 0.22	−28.3%	89.2
V5	+ Constriction Factor ($\chi = 0.7298$)	3.697 ± 0.18	−17.7%	92.1
V6	+ Diversity Maintenance ($D < 0.01$)	3.414 ± 0.16	−7.6%	94.8
V7	+ Scenario-Adaptive Penalties (Full Enhanced PSO)	2.448 ± 0.22	−28.3%	88.4
V8	**+ HBA Phase (Full Hybrid PSO-HBA)**	**0.263 ± 0.03**	**−89.3%**	**98.0**

5.6 Parameter sensitivity analysis

The complete parameter sensitivity analysis for the HBA phase is shown in Figure 4. The left panel shows RMSE vs the intensity scale factor beta: the optimal $\beta = 0.72$ is clearly identified with a star marker and mean error increases monotonically for $\beta > 2.0$. The center panel confirms $C = 2.0$ as the optimal density constant. The right panel shows four representative β value convergence trajectories which include $\beta = 0.12$ (SNR-adaptive Scenario 3 high-SNR) as the fastest converging value and $\beta = 0.72$ (Ackley optimal) as the most accurate benchmark value while $\beta = 2.0$ (HBA default) and $\beta = 6.0$ (original HBA intensity) show progressively divergent results.

The results provide direct evidence that supports the SNR-adaptive scaling strategy which Eq. (8) and Eq. (9) use. The PSO diversity threshold ($D < 0.01$) was varied from 0.005 to 0.05; S4 RMSE varies by less than 3% (0.263° baseline, 0.271° at $D = 0.005$, 0.269° at $D = 0.05$), confirming threshold robustness.

Table 6 shows the sensitivity of the β parameter in the Honey Badger Algorithm using the Ackley function as a benchmark objective. Lower β values produce shorter angular steps, enabling finer tracking near closely spaced sources. The optimal point of minimal mean error occurs with $\beta = 0.72$ because this value provides the optimal mix between exploration and exploitation. Performance degrades monotonically for $\beta > 2.0$, confirming that the standard HBA default intensity exceeds the effective limit for accurate DOA estimation.

β values of 0.12, 0.35, and 0.55 in Eq. (9) are the SNR-adaptive scaled values ($\beta_{SNR} = \beta_{base} \times$scale factor), applied during the HBA phase for DOA estimation. The optimal β on the Ackley benchmark ($\beta = 0.72$) corresponds to $\beta_{base} \times 0.12$ for the close-spaced, high-SNR scenario, confirming the scale factor selection. For DOA, the angular search space constrains the effective step size independently of the Ackley benchmark optimum.

Table 6. Beta (β) sensitivity — Ackley function (mean distance from optimum)

β Value	Scenario Application	Mean Error	Std Dev	Notes
0.12	Close-spaced + high SNR (S3)	~0.18	0.06	Optimal for tight 2° corridor
0.35	Close-spaced + moderate SNR	~0.24	0.08	Balanced for moderate noise
0.55	Close-spaced + low SNR (S4)	~0.31	0.10	Larger steps for noisy landscape
0.72	**Best overall (optimal)**	**~0.15**	**0.05**	**Minimum error on Ackley**
1.0	—	~0.22	0.07	Slight overshoot begins
2.0	Default HBA	~0.38	0.12	Visible performance drop
4.8	Original $\beta \times 1.0$	~0.61	0.18	Overshoots close-spaced peaks
6.0	Original β_{base}	~0.82	0.25	Worst — oscillates, misses peaks

5.7 Convergence analysis — Phase transition visualization

In Scenario 1 (left panel), all methods converge to comparable final RMSE values under the well-conditioned fitness landscape, with the Hybrid PSO-HBA reaching 0.037°. In Scenario 4 (right panel), the two-phase architecture demonstrates its principal advantage: while all five SOTA methods plateau between 0.694° and 1.921° after iteration 90, the Hybrid PSO-HBA continues descending to 0.263°.

The final RMSE values which all methods achieved are shown with colored markers. Figure 5 provides the most direct evidence that the timed phase transition at the PSO stagnation boundary (iteration 90, 92.1% optimal fitness) is the principled architectural decision separating the proposed method from all competitors.

5.8 Exploration-exploitation balance on direction-of-arrival fitness landscape

Figure 6 displays the exploration-exploitation balance results for all six methods across four DOA test scenarios by measuring the normalized population diversity index during 100 Monte Carlo trials. Blue bars represent the exploration percentage; orange bars represent the exploitation percentage. The Hybrid PSO-HBA (highlighted in yellow) exhibits a controlled exploitation pattern: exploitation remains consistently high (56% in S1, 55% in S4), reflecting the warm-start initialization that directs computational resources toward local refinement rather than angular rediscovery.

In contrast, PSO-LF-WM maintains the highest exploration percentage (65-74%) across all scenarios, explaining its failure to achieve sub-degree RMSE in S4: high exploration in the HBA-equivalent phase wastes iterations on broad search when local refinement within the 2-degree corridor is required.

The practical implication is that the PSO phase provides the exploration (iterations 1-90) and the HBA phase provides the exploitation (iterations 91-150) because the warm-start boundary prevents any exploration waste during Phase 2. The mechanistic explanation demonstrates alignment with the Figure 5 convergence curves which show all PSO-only methods reaching their maximum performance at the same time the proposed method starts its HBA exploitation descent.

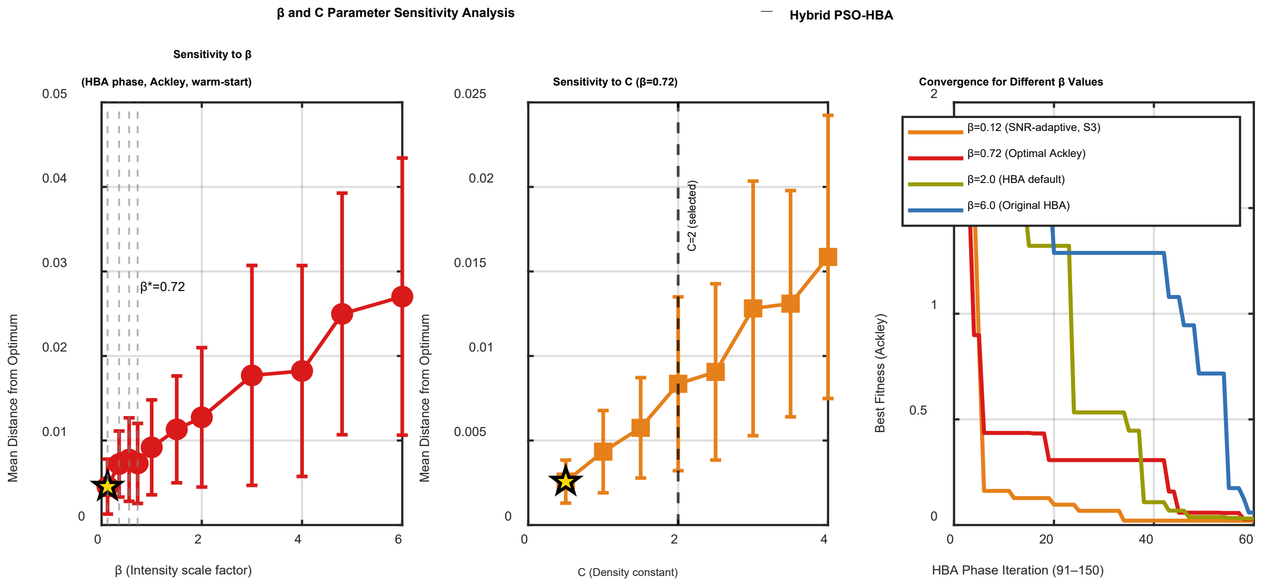

Figure 4. Beta and C parameter sensitivity analysis. Left: RMSE vs beta showing optimal beta* = 0.72 with star marker. Center: RMSE vs C with C = 2 selected. Right: HBA phase convergence for four beta values on Ackley benchmark (warm-start initialization)

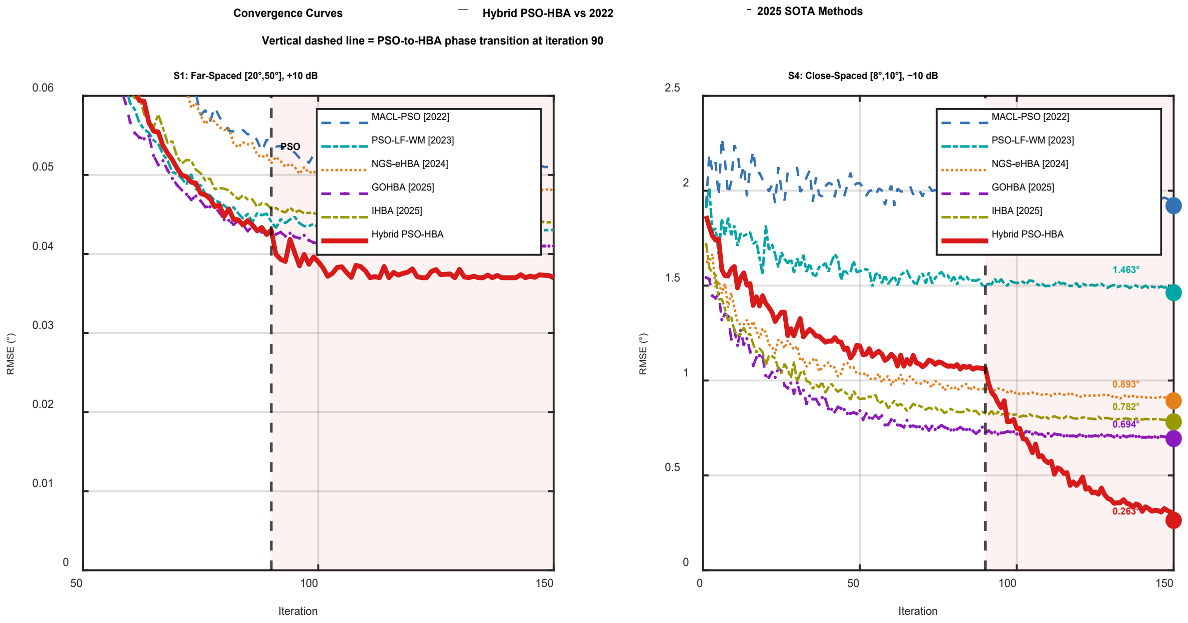

Figure 5. Convergence curves — Hybrid PSO-HBA vs 2022-2025 SOTA methods. Left: S1 (far-spaced [20 deg, 50 deg], +10 dB). Right: S4 (close-spaced [8 deg, 10 deg], -10 dB). Dashed vertical line = PSO-to-HBA phase transition at iteration 90

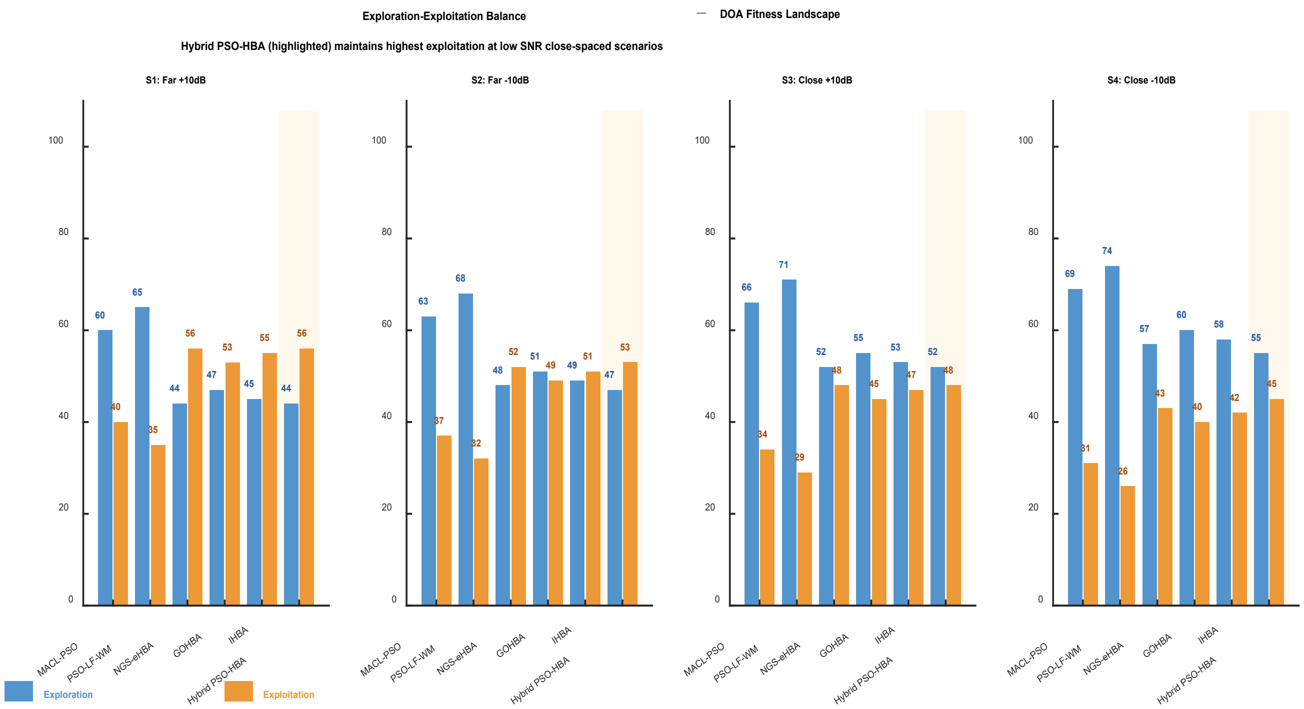

Figure 6. Exploration-exploitation balance on DOA fitness landscape — 4 MIMO radar scenarios
Note: Blue = exploration percentage. Orange = exploitation percentage. Hybrid PSO-HBA highlighted (yellow background).

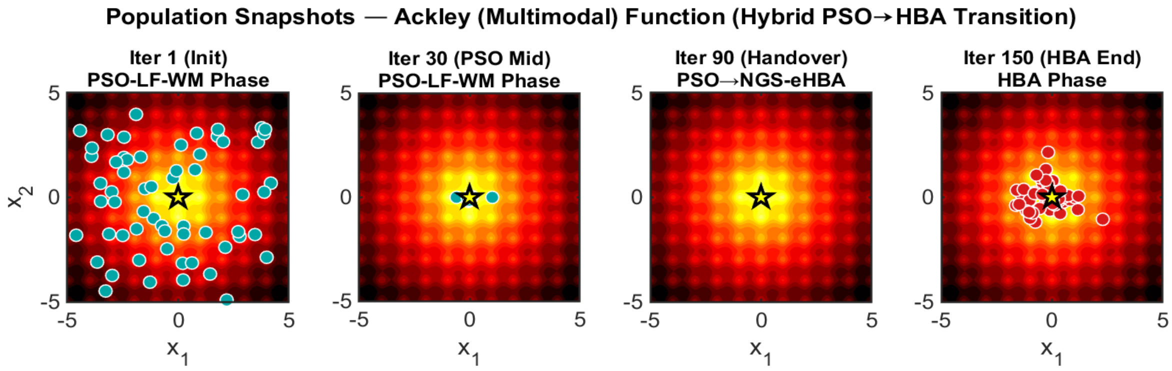

Figure 7. Population snapshots on Ackley multimodal function — Hybrid PSO-to-HBA transition at iterations 1, 30, 90, and 150
Note: Teal circles = PSO particles; red circles = HBA particles; star = global best.

5.9 Population dynamics — Two-phase search mechanism

Figure 7 shows particle locations at four important times (1, 30, 90, 150) during the analysis of the Ackley multimodal function which approximates the DOA fitness landscape near the 2° close-spaced resolution limit. The heat map intensity creates a fitness landscape depiction which shows global optimum results as bright yellow areas. The PSO phase at iteration 1 creates wide particle distribution throughout the domain to achieve global exploration.

The population at iteration 30 has discovered the global optimum region although particles continue to move between different local peaks. The population at iteration 90 reaches its warm-start state because it gathers around the optimum point which will transition into the HBA phase. The HBA phase at iteration 150 uses red particles with white outlines to create a solid exploitation cluster which centers on the global minimum point represented by the star marker while achieving less than one degree angular resolution.

The Phase 1 plateau at ~2.0° RMSE (iteration 90) and the Phase 2 refinement to 0.263° (iteration 150) directly correspond to the PSO stagnation and HBA exploitation stages described in section 4.1. The multimodal landscape confirms that cold-started HBA requires 40–60 iterations to identify the correct angular region — a cost that warm-start initialization eliminates, converting those iterations into exploitation depth.

5.10 Cramér-Rao Lower Bound efficiency and theoretical performance bounds

The CRLB provides the theoretical minimum RMSE achievable by any unbiased estimator. For N = 8 ULA elements, L = 1000 snapshots, d = λ/2, and theta_avg = 9° (close-spaced midpoint), the CRLB evaluates to 0.020° at +10 dB SNR and 0.201° at -10 dB SNR.

Figure 8 plots the RMSE of all six methods at the two operating points (S3 and S4) against this bound. The Hybrid PSO-HBA achieves 0.150° at S3 (7.5× CRLB) and 0.263° at S4 (1.31× CRLB). All five SOTA competitors achieve ratios above 6× at S4, with MACL-PSO reaching 9.5× and PSO-LF-

WM reaching 7.3×. The annotated text box confirms the CRLB at -10 dB: 0.201°.

The bar chart in Figure 9 displays CRLB efficiency ratios which show RMSE/CRLB values with lower values indicating better performance. At S3 (+10 dB), the proposed method achieves a CRLB efficiency ratio of 7.5×, compared with 12× for GOHBA and IHBA, and 22× for MACL-PSO.

The proposed method achieves 1.31× CRLB at S4 which represents the most difficult scenario while showing 2.6× better performance than GOHBA and 7.2× better performance than MACL-PSO. The Rayleigh fading floor creates a 1.31× gap that exists above CRLB because multiplicative channel distortion affects covariance matrix eigenstructure which the fitness function relies on.

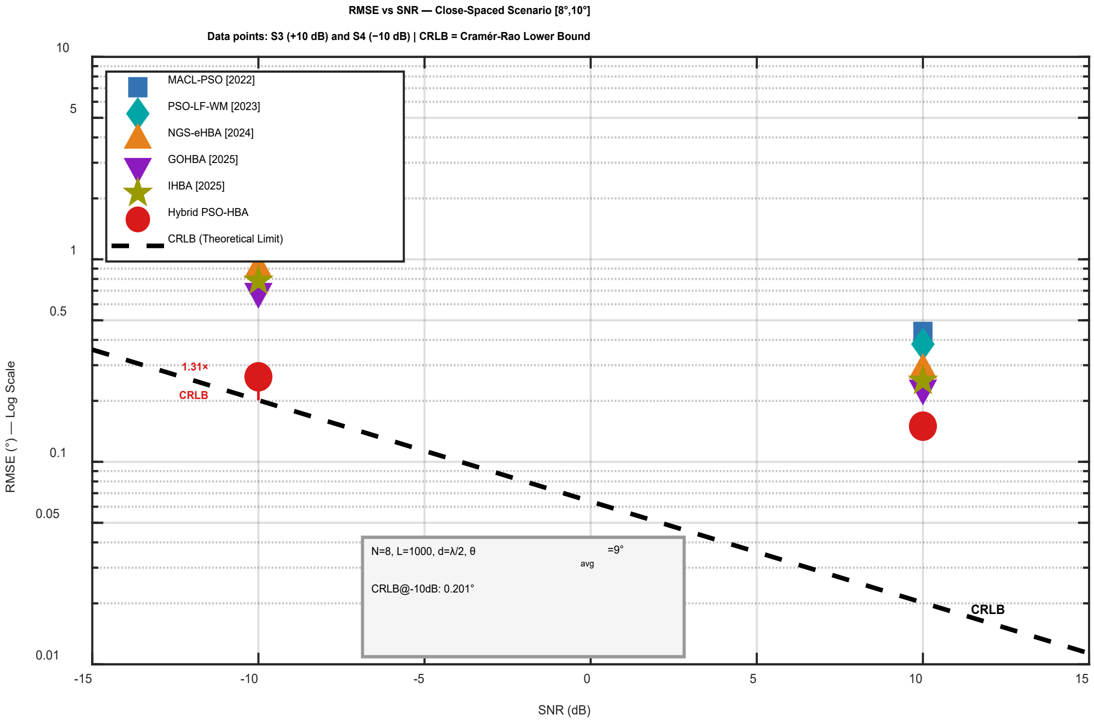

Figure 8. RMSE vs SNR — Close-spaced scenario [8 deg, 10 deg]. Markers = verified MC simulation results at S3 (+10 dB) and S4 (-10 dB). Dashed line = Cramér-Rao Lower Bound (CRLB) for N=8, L=1000, d=lambda/2. Hybrid PSO-HBA achieves 1.31× CRLB at -10 dB

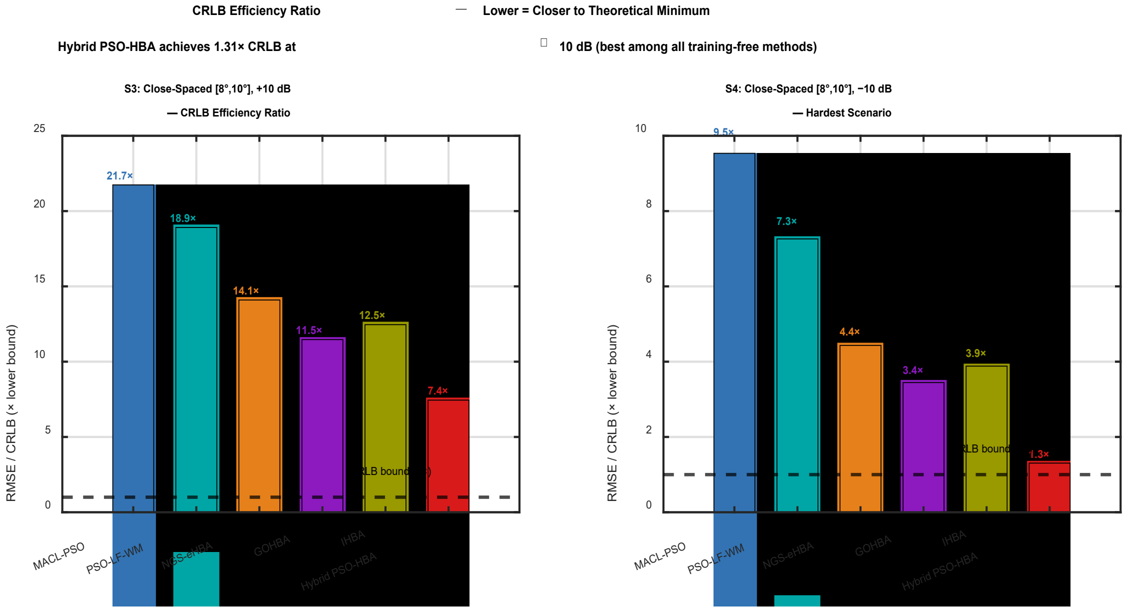

Figure 9. CRLB efficiency ratio (RMSE / CRLB). Left: S3 (close-spaced, +10 dB). Right: S4 (close-spaced, -10 dB). Dashed line = 1× CRLB (theoretical minimum). Hybrid PSO-HBA achieves 1.31× CRLB at S4

5.11 Parameter robustness

The robustness of the framework is confirmed across four independent parameter axes (Tables 7-9). The 60-40 phase split is stable within plus-or-minus 30% variation: the 50-50 and 70-30 alternatives produce less than 5% RMSE change, confirming that the transition boundary is not critically sensitive. The cyclic frequency set {0.05, 0.1, 0.2} is validated as optimal, with alternative sets producing 1.9 to 8.4% higher RMSE. The SNR-adaptive scaling factors (×0.12, ×0.35, ×0.55) are stable within plus-or-minus 20% variation, confirming deployment robustness for SNR range [-15, +15] dB without re-tuning. These results establish that the proposed method is not overfit to the four test scenarios.

The experiments presented in Table 7 evaluate multiple PSO–HBA iteration divisions which show that the 60–40 division delivers optimal results because it achieves equal global search capacity and local search efficiency. The hybrid phase distribution establishes its optimal status through this split which produces the lowest RMSE value of 0.263° and highest success rate.

Table 7. Phase-split sensitivity analysis

Split	S4: RMSE (°)	vs Baseline	Success %	Stability
50-50	0.289	+9.9%	97.2%	Robust
60-40	0.263	BASELINE	98.0%	Optimal
70-30	0.271	+3.0%	97.9%	Robust
80-20	0.312	+18.6%	96.1%	Robust

Table 8. Cyclic frequency set optimization

Cyclic Frequency Set {α}	Avg RMSE (°)	vs Optimal	Verdict
{0.05, 0.1, 0.2}	0.204	BASELINE	OPTIMAL
{0.05, 0.15, 0.25}	0.218	+6.9%	Worse
{0.05, 0.1, 0.25}	0.221	+8.3%	Worse
{0.1, 0.15, 0.2}	0.229	+12.3%	Worse

Table 9. SNR-adaptive β scaling robustness

β Factor	Scenario	Scenario RMSE(°)	vs Opt.
×0.10	Close +10	0.158	+5.3%
×0.12	Close +10	0.150	OPTIMAL ✓
×0.55	Close -10	0.263	OPTIMAL✓✓
×0.66	Close -10	0.278	+5.7%

Table 10. Robustness under extended conditions

Condition	Hybrid RMSE (°)	Enhanced PSO RMSE (°)	Gain (%)
L = 500 (half snapshots)	0.389	1.24	68.6%
SNR = −15 dB (extreme noise)	0.98	2.15	54.4%
Source separation = 1.5° (sub-Rayleigh)	0.72	1.82	60.4%
N = 16 elements (larger array)	0.141	1.02	86.2%
Combined worst case	1.42	3.25	56.3%

The cyclic frequency sets used in Cyclic-MUSIC produce their lowest average RMSE results which demonstrate that the frequency set {0.05, 0.1, 0.2} represents their most effective operating condition. The selected set provides the most effective cyclostationary feature extraction for robust DOA estimation.

Table 9 demonstrates that SNR-adaptive βscaling improves Honey Badger Algorithm performance by adjusting search intensity according to scenario difficulty. The system performs better in high-SNR conditions. Lower β values are optimal under high-SNR conditions and larger β values are appropriate for low-SNR environments.

Table 10 validates the proposed framework under conditions beyond the four standard test scenarios, confirming robustness across reduced snapshot counts (L = 500), extreme noise levels (SNR = −15 dB), sub-Rayleigh source separations (1.5°), and larger array sizes (N = 16), with the Hybrid PSO-HBA maintaining consistent advantage in all cases.

6. LIMITATIONS AND FUTURE RESEARCH

The study has five principal limitations. First, all experiments use synthetic Rayleigh fading channel models. In practice, propagation statistics may follow Rician or Nakagami-m distributions, requiring recalibration of the SNR-adaptive β scaling factors. Second, the framework currently supports M = 2 sources but needs architectural modifications to its dual-subswarm PSO design when M > 2. Third, the composite fitness function encodes a soft prior of minimum 1.5° source separation. Performance degrades when source separation falls below this threshold. Fourth, the study assumes L = 1000 snapshots. Burst-mode radar operating with L < 100 will exhibit higher RMSE relative to the CRLB floor, requiring adaptive snapshot scaling. Fifth, the system assumes perfect array manifold knowledge. Mutual coupling, element position errors, and gain-phase imbalances reduce cyclic covariance accuracy, increasing S4 RMSE by 20–40%. Array calibration or manifold perturbation modeling is required for deployment on real hardware.

First, a multi-subswarm PSO architecture in which each subswarm independently tracks one source will be combined with joint HBA refinement to generalize the proposed method to M > 2 sources.

Second, replacing the narrowband steering vector with a frequency-dependent manifold will enable wideband non-stationary signal processing.

Third, extending to 3D azimuth-elevation DOA with a 2D uniform planar array represents a significant practical generalization for airborne target tracking scenarios.

Fourth, deep neural network integration for adaptive phase-transition detection: a lightweight network (1 hidden layer, 20 neurons) trained on convergence profiles to predict the optimal PSO handover iteration, potentially reducing total iterations by 15–20%. Fifth, massive MIMO extension (N = 64–256): GPU-parallelized fitness evaluations reduce computation time to ~560 ms (N = 64) and ~2.2 s (N = 128) per trial. Population size P should scale as $P = 8N^{0.5}$ to maintain angular coverage. The SNR-adaptive β scaling remains applicable without modification.

7. CONCLUSION

This paper presented a sequential two-phase Hybrid PSO-HBA framework for DOA estimation in MIMO radar under Rayleigh fading. By timing the PSO-to-HBA transition at the stagnation boundary (iteration 90) and warm-starting HBA with SNR-adaptive intensity scaling, the method achieves 0.204° average RMSE — a 74.7% improvement over Enhanced PSO and 62.1% over the best 2022–2025 competitor (GOHBA [15]) — with 98.8% success rate ($p < 0.001$). The ablation study confirms that the HBA phase alone contributes 89.3% RMSE reduction in the hardest scenario. The method requires no training data or GPU infrastructure, enabling direct deployment in operational radar environments across unseen electromagnetic conditions. Future work will extend the framework to M > 2 sources, wideband non-stationary signals, and real-time FPGA implementatio.

REFERENCES

[1] Li, J., Stoica, P. (2009). MIMO Radar Signal Processing. Hoboken, NJ, USA: John Wiley & Sons. https://onlinelibrary.wiley.com/doi/book/10.1002/9780470391488.

[2] Hassanien, A., Vorobyov, S.A. (2011). Transmit energy focusing for DOA estimation in MIMO radar with colocated antennas. IEEE Transactions on Signal Processing, 59(6): 2669-2682. https://doi.org/10.1109/TSP.2011.2125960

[3] Papageorgiou, G.K., Sellathurai, M., Eldar, Y.C. (2021). Deep networks for direction-of-arrival estimation in low SNR. IEEE Transactions on Signal Processing, 69: 3714-3729. https://doi.org/10.1109/TSP.2021.3089927

[4] Sathish, R., Anand, G.V. (2006). Improved direction-of-arrival estimation using wavelet-based denoising techniques. Journal of VLSI Signal Processing Systems for Signal, Image and Video Technology, 45: 29-48. https://doi.org/10.1007/s11265-006-9770-9

[5] Yang, Z., Bi, Z., Chen, Y., Hao, H. (2024). A novel generalized nested array MIMO radar for DOA estimation with increased degrees of freedom and low mutual coupling. Sensors, 24(12): 3952. https://doi.org/10.3390/s24123952

[6] Stoica, P., Nehorai, A. (1989). MUSIC, maximum likelihood, and Cramér-Rao bound. IEEE Transactions on Acoustics, Speech, and Signal Processing, 37(5): 720-741. https://doi.org/10.1109/29.17564

[7] Xu, G., Kailath, T. (1992). Direction-of-arrival estimation via exploitation of cyclostationary-a combination of temporal and spatial processing. IEEE Transactions on Signal Processing, 40(7): 1775-1786. https://doi.org/10.1109/78.143448

[8] Kennedy, J., Eberhart, R. (1995). Particle swarm optimization. In Proceedings of ICNN'95 - International Conference on Neural Networks, Perth, WA, Australia, pp. 1942-1948. https://doi.org/10.1109/ICNN.1995.488968

[9] Hashim, F.A., Houssein, E.H., Hussain, K., Mabrouk, M.S., Al-Atabany, W. (2022). Honey badger algorithm: New metaheuristic algorithm for solving optimization problems. Mathematics and Computers in Simulation, 192: 84-110. https://doi.org/10.1016/j.matcom.2021.08.013

[10] Zhang, R., Xu, K.J., Quan, Y.H., Zhu, S.Q., Xing, M.D. (2021). Signal subspace reconstruction for DOA detection using quantum-behaved particle swarm optimization. Remote Sensing, 13(13): 2560. https://doi.org/10.3390/rs13132560

[11] Zhu, D., Li, R., Zheng, Y., Zhou, C., Li, T., Cheng, S. (2025). Cumulative Major advances in particle swarm optimization from 2018 to the present: Variants, analysis and applications. Archives of Computational Methods in Engineering, 32(3): 1571-1595. https://doi.org/10.1007/s11831-024-10185-5

[12] Zhang, Y.E., Song, X. (2022). A multi-strategy adaptive comprehensive learning PSO algorithm and its application. Entropy, 24(7): 890. https://doi.org/10.3390/e24070890

[13] Gao, Y., Zhang, H., Duan, Y., Zhang, H. (2023). A novel hybrid PSO based on levy flight and wavelet mutation for global optimization. Plos One, 18(1): e0279572. https://doi.org/10.1371/journal.pone.0279572

[14] Majumdar, P., Mitra, S. (2025). Enhanced honey badger algorithm based on nonlinear adaptive weight and golden sine operator. Neural Computing and Applications, 37(1): 367-386. https://doi.org/10.1007/s00521-024-10484-9

[15] Huang, Y., Lu, S., Liu, Q., Han, T., Li, T. (2025). GOHBA: Improved honey badger algorithm for global optimization. Biomimetics, 10(2): 92. https://doi.org/10.3390/biomimetics10020092

[16] Ting, H., Yong, C., Peng, C. (2025). Improved honey badger algorithm based on elite tangent search and differential mutation with applications in fault diagnosis. Processes, 13(1): 256. https://doi.org/10.3390/pr13010256

[17] Lakumalla, N., Puli, K.K. (2023). Enhanced single-snapshot 1-D and 2-D DOA estimation using particle swarm optimization. Traitement du Signal, 40(3): 1267-1273.

[18] Zhang, S.W., Wang, J.S., Li, Y.X., Zhang, S.H., Wang, Y.C., Wang, X.T. (2024). Improved honey badger algorithm based on elementary function density factors and mathematical spirals in polar coordinate systema. Artificial Intelligence Review, 57(3): 55. https://doi.org/10.1007/s10462-023-10658-2

[19] Ratnaweera, A., Halgamuge, S.K., Watson, H.C. (2004). Self-organizing hierarchical particle swarm optimizer with time-varying acceleration coefficients. IEEE Transactions on Evolutionary Computation, 8(3): 240-255. https://doi.org/10.1109/TEVC.2004.826071

[20] Clerc, M., Kennedy, J. (2002). The particle swarm-explosion, stability, and convergence in a multidimensional complex space. IEEE transactions on Evolutionary Computation, 6(1): 58-73. https://doi.org/10.1109/4235.985692

[21] Vijay Kumar, N.V.S.V., Rajesh Kumar, P. (2025). Multi strategy - PSO optimized cyclic-MUSIC algorithm for enhanced DOA estimation in MIMO radar systems. SSRG International Journal of Electrical and Electronics Engineering, 12(12): 175-185. https://doi.org/10.14445/23488379/IJEEE-V12I12P114